Check for updates

Research Article Vol. 38, No. 10 / October 2021 / *Journal of the Optical Society of America A* **B19**

Journal of the Optical Society of America A
OPTICS, IMAGE SCIENCE, AND VISION

Fourier-basis structured illumination imaging with an array of integrated optical phased arrays

Nathan Dostart,[1,2,*] Bohan Zhang,[3] Michael Brand,[1] Daniel Feldkhun,[1] Miloš Popović,[3] and Kelvin Wagner[1]

[1] *Department of Electrical, Computer, and Energy Engineering, University of Colorado Boulder, Boulder, Colorado 80309, USA*
[2] *Current address: NASA Langley Research Center, Hampton, Virginia 23681, USA*
[3] *Department of Electrical and Computer Engineering, Boston University, Boston, Massachusetts 02215, USA*
**Corresponding author: nathan.a.dostart@nasa.gov*

Received 5 May 2021; revised 22 July 2021; accepted 27 July 2021; posted 27 July 2021 (Doc. ID 430600); published 20 August 2021

Active imaging and structured illumination originated in "bulk" optical systems: free-space beams controlled with lenses, spatial light modulators, gratings, and mirrors to structure the optical diffraction and direct the beams onto the target. Recently, optical phased arrays have been developed with the goal of replacing traditional bulk active imaging systems with integrated optical systems. In this paper, we demonstrate the first array of optical phased arrays forming a composite aperture. This composite aperture is used to implement a Fourier-based structured-illumination imaging system, where moving fringe patterns are projected on a target and a single integrating detector is used to reconstruct the spatial structure of the target from the time variation of the back-scattered light. We experimentally demonstrate proof-of-concept Fourier-basis imaging in 1D using a six-element array of optical phased arrays, which interfere pairwise to sample up to 11 different spatial Fourier components, and reconstruct a 1D delta-function target. This concept addresses a key complexity constraint in scaling up integrated photonic apertures by requiring only N elements in a sparse array to produce an image with N^2 resolvable spots.

https://doi.org/10.1364/JOSAA.430600

1. INTRODUCTION

Integrated optical phased arrays (OPAs) have been the subject of intense recent research to enable high-speed, small form-factor beam-steering systems for automotive LIDAR applications [1]. There have been many demonstrated integrated OPAs [2–19], and the field continues to grow rapidly. Beam steering with OPAs enables spatially resolved measurements of intensity (imaging) and/or range (LIDAR). The standard approach to imaging with OPAs so far [5,9,10,13] has been beam steering through a 2D array of angles for raster scan imaging: ideally, the OPA forms a near diffraction-limited beam which illuminates (and/or receives from) a single resolvable spot of the target at a time. This spot is scanned across the field of view (FOV) of the OPA while the range is measured from the time-of-flight delay that is extracted from a back-scattered signal for each transmitted beam. A single detector coupled to collecting optics or an OPA is therefore sufficient to perform imaging. More advanced imaging schemes, however, could be used to realize new and improved imaging modalities. One such recent demonstration [12] used a "ghost imaging" [20] setup with a compressive sensing [21] approach to reconstruct an image without correcting for unknown emitter phases prior to illumination. This demonstration highlights the potential advantages of applying active imaging approaches to OPAs.

Recent OPA demonstrations have utilized aperiodic [8] and sparse [11] emitter layouts to suppress grating lobes [22] and ease routing complexity [11]. Just as the periodic spacing of emitters in OPAs creates grating lobes, analogous "tiling lobes" arise for periodic arrays of OPAs [17] which require similar compensation techniques. However, sparse layouts have other advantages which have yet not been explored in the OPA literature, such as the potential to intersperse transmitters and receivers, minimize cross-talk, and reduce the number of emitters required to achieve a certain spatial resolution. In particular, a well-chosen sparse array with N elements can achieve the same resolution as a fully populated array with N^2 elements [23]. Imaging techniques designed for sparse OPAs, or sparse arrays of OPAs, are necessary to fully leverage these advantages.

Synthesis imaging in radio astronomy has developed extensive passive imaging techniques for extremely sparse arrays that can be used as inspiration for active OPA transmitter and receiver architectures. In interferometric synthesis imaging, a set of up to $N(N-1)/2$ baselines (spatial frequencies) from interferometric pairings of N RF receivers provide Fourier domain samples of the spatial frequency associated with each unique baseline. This type of Fourier domain approach thereby samples $O(N^2)$ image degrees of freedom with only N receivers. Many of these techniques have already been used in the optical domain, such as Fourier telescopy [24,25] and the CHIRPT method [26]. An in-depth discussion of optical sparse aperture techniques can be found in [23]. Sparse aperture imaging with integrated photonics has been discussed [27] and demonstrated [28] using this multi-baseline receiver architecture.

We build on these sparse-array interferometric receiver concepts using an alternative approach based on *illuminating* the target with multiple baselines to create a non-redundant set of moving fringes, in particular using OPAs to generate the illumination and collect the back-scattered light. This illumination technique, previously proposed in the bulk optics domain in the context of microscopy [29], is referred to as Fourier-basis agile structured illumination and sensing ($\mathcal{F}$-BASIS). Encoding each fringe pattern onto a unique RF tone [30] allows for the simultaneous illumination with *all* fringes generated by pairwise interference for fast image acquisition of a sparse subset of a target's Fourier domain representation. In addition to the fast image acquisition capability, $\mathcal{F}$-BASIS is compatible with a set of self-calibration algorithms developed for radio astronomy [31,32] which are capable of correcting for unknown emitter phases. These unknown phases are the Achilles' heel of, and a major challenge to, the practical scaling of current OPA demonstrations to large apertures comprised of arrays of OPAs. These self-calibration algorithms do not require a "guiding star," or additional calibration circuitry, using only the measured return signals to correct for the unknown phases of each emitter. Even in the absence of phase errors, these algorithms can iteratively improve the image reconstruction by filling in unmeasured Fourier coefficients that help fulfill *a priori* image constraints [32]. This active imaging technique is therefore robust to phase errors and includes self-correcting capabilities, taking full advantage of advanced calibration algorithms to maximize the OPA imaging performance.

In this work, we use a 1D sparse array of OPAs as an agile illumination source for a proof-of-concept of $\mathcal{F}$-BASIS imaging that could be extended to a larger sparse, non-redundant 2D array of transmit tiles for a practical lidar imaging aperture. The OPAs are passive 2D wavelength-steered serpentine OPAs (SOPAs) demonstrated previously [17,33]. We present the general $\mathcal{F}$-BASIS scheme and develop a version applicable to both single-OPA and arrayed-OPA (tiled aperture) imaging. Implementing $\mathcal{F}$-BASIS with OPAs is discussed, as well as details on the particular OPA design used in this work. We demonstrate image reconstruction of a delta-function 1D target (narrow opaque strip) using six OPAs composing an 11-baseline $\mathcal{F}$-BASIS interferometric illumination system with simple incoherent detection. Experiments show that the strip target, which cannot be resolved by a single OPA, is approximately resolved by the $\mathcal{F}$-BASIS approach to demonstrate an 11× resolution enhancement over a single OPA. This first demonstration of multi-OPA imaging shows the potential for OPAs to benefit from the techniques of active computational imaging, as well as the suitability of OPAs as illumination sources in a new generation of imaging technologies.

2. FOURIER-BASIS IMAGING

We first introduce the envisioned imaging system utilizing a hierarchical active imaging scheme with a "tiled aperture" [17,34] composed of an array of OPAs. A single OPA can address a 2D array of spots using traditional beam-steering, as shown in Fig. 1(a). Utilizing an array of such OPAs to form a tiled aperture, a higher resolution can be achieved by emitting from multiple OPAs simultaneously. We propose a novel bi-static scheme, utilizing separate transmitters and receivers, where both transmit and receive apertures are interleaved into the same aperture area [Fig. 1(b), top].

In this scheme, an N^2 array of OPAs includes both transmit and receive elements, where $O(N)$ OPAs emit simultaneously to illuminate the target and $O(N^2)$ OPAs are used as receivers. The incorporation of a bi-static architecture into a single aperture allows for compact packing and efficient use of chip (and aperture) footprint. The pairwise interference of transmitter OPAs projects fringe patterns onto the target with periodicity and orientation determined by the spatial separation of each pair within the transmit array [Fig. 1(b), bottom] allowing $\mathcal{F}$-BASIS imaging of the target within the spot projected onto the target by a single OPA. The first demonstration of such sub-spot imaging

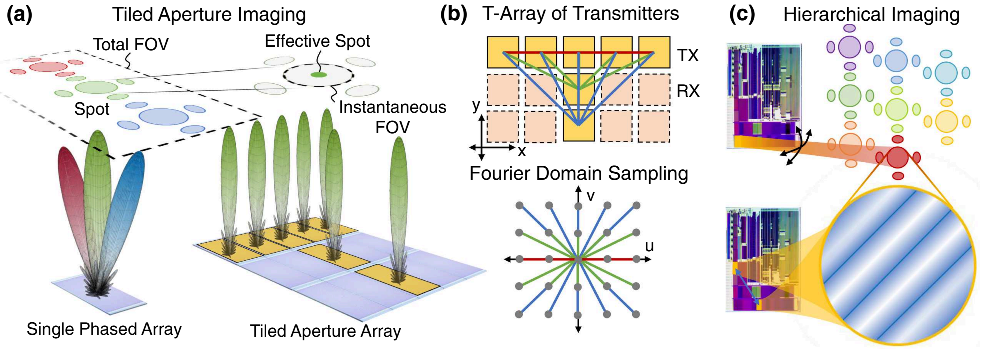

Fig. 1. Hierarchical imaging with arrays of phased arrays. (a) A single phased array addresses a large FOV with low resolution using traditional beam-steering (here, with wavelength denoted by the red, green, and blue beams/spots). A composite aperture, which we term a "tiled aperture," composed of multiple such OPAs (in this case in a T-shape) transmitting simultaneously can increase both the resolution and collected power. The increased resolution afforded by $\mathcal{F}$-BASIS is denoted by the green effective spot; the instantaneous FOV is denoted by a dashed line and corresponds to the spot size of a single OPA. (b) Transceiver scheme where a bi-static aperture (separate transmit and receiver optics) is implemented with a single array. A T-shaped subset of the OPAs transmit (gold, solid outline) and interfere pairwise to sample the target in the Fourier domain (bottom). The remaining OPAs in the array are used as receivers (orange, dashed outline). (c) Hierarchical imaging scheme combining raster scanning for a large FOV (top) and "super-resolved" imaging within a single raster scan spot (bottom) using the $\mathcal{F}$-BASIS scheme described in this paper.

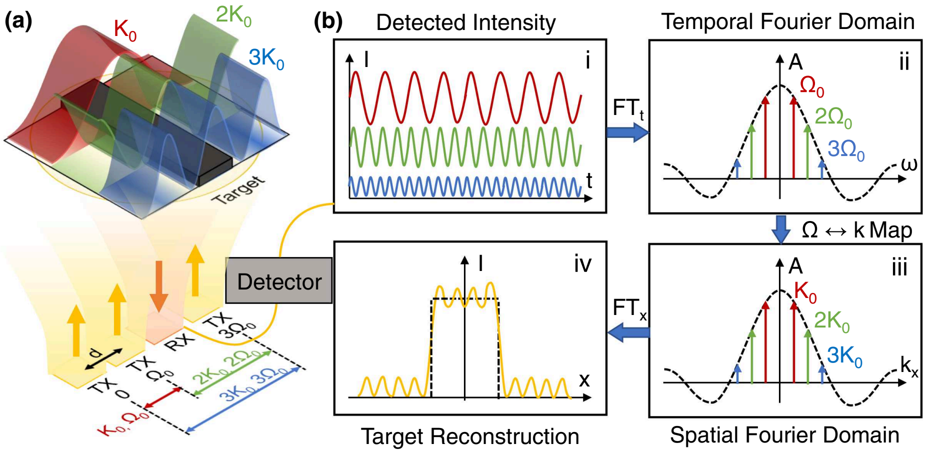

Fig. 2. $\mathcal{F}$-BASIS concept with an example 3 transmitter (TX)/1 receiver (RX) OPA array. (a) Simultaneous illumination of the target with all OPAs, with non-redundant spacing in both spatial and frequency domains, creates moving fringes on the target (red, green, blue). Each fringe pattern has a unique spatial and temporal frequency ($K_i \leftrightarrow \Omega_i$). (b) Image reconstruction approach: (i) the detected intensity simultaneously measures the amplitude and phase of every beat note; (ii) a temporal Fourier transform enables all these beat notes to be separated; (iii) the spatio-spectral mapping, $K_i \leftrightarrow \Omega_i$, determines which "pixels" in the Fourier domain to populate with the measured complex amplitudes; (iv) an inverse spatial Fourier transform, or appropriate algorithm, reconstructs the real-space target image.

is the subject of this paper. The increased resolution afforded by $\mathcal{F}$-BASIS is part of the overall (hierarchical) imaging scheme which benefits from the large FOV provided by an individual OPA [Fig. 1(c), top] while simultaneously offering high resolution using $\mathcal{F}$-BASIS [Fig. 1(c), bottom]. This hierarchical approach is compatible with foveated (region of interest) imaging, where increased resolution is only obtained in the desired location(s), allowing for precious photons and processing power to be spent in the most efficient manner possible. While this hierarchical approach provides our overarching scheme for imaging with an array-of-arrays, we focus in this paper on resolution enhancement using $\mathcal{F}$-BASIS within the spot of a single OPA. Additional discussion on the hierarchical imaging scheme can be found in Supplement 1.

Resolution enhancement is presented in Fig. 2 with a simple example architecture. Here, all OPAs emit to the same angle coherently such that their spots overlap in the far field. For wavelength-steered OPAs such as the SOPAs used in this paper, this corresponds to all OPAs emitting at the same wavelength. The system is shown in Fig. 2(a) where a minimal, 1D non-redundant array [35] with three transmitters (TX) projects a set of three unique fringe patterns (baselines, in radio astronomy parlance) onto a target in the far field. For larger arrays of N transmitters, the number of pairwise interferometric fringes grows quadratically with N and up to $N(N-1)/2$ unique fringe patterns can be obtained using a non-redundant array. A receiver (RX) collects back-scattered light from the target for detection. In a larger $N \times N$ array, multiple RX OPAs can be used to increase power collection within the same array footprint, but do not otherwise affect system performance. Notably, multiple RX OPAs, each coupled to a separate detector which are then current-summed, can result in increased power without speckle loss associated with coherent detection (see [17], Supplement 1).

The four-element array spaced with period d has three non-redundant "slots" ($[0, 1, 3] \times d$) populated with TX OPAs and one slot ($[2] \times d$) with a single RX OPA. Each TX OPA is shifted in temporal frequency relative to the input laser by a non-redundant shift ($[0, 1, 3] \times \Omega_0$) chosen so that the difference frequency for each pair is unique, making a non-redundant array in the frequency domain as well. For 2D sparse spatially non-redundant arrays, the mapping of RF frequencies to spatial frequencies is more complex than the demonstrative 1:1 mapping in this example. Each pair of TX OPAs projects a moving fringe pattern onto the target, and the use of non-redundant spatial and spectral spacings ensures each fringe pattern has a unique spatial frequency and temporal beat frequency. For example, the OPAs at locations [0,1] create a fringe pattern with a spatial periodicity $K_0 = 2\pi d/\lambda z$ and beat frequency Ω_0 (red). The other TX OPA pairings create similarly unique fringe patterns: [1,3] creates a spatial periodicity $2K_0$ at $2\Omega_0$ (green) and [0, 3] creates a spatial periodicity $3K_0$ at $3\Omega_0$ (blue). All fringe patterns scroll across the target at a velocity $v_i = \Omega_i/K_i$. The spatial and frequency spacings shown for this example are only a small subset of many potential array choices, which might be non-redundant (all spatial and temporal frequencies are unique) or "semi-redundant" (containing some number of redundant frequencies in spatial and/or spectral domains). See Supplement 1 for additional discussion. An example integrated photonic implementation of this system would use a single laser, split equally three ways to the TX OPAs. The TX OPAs would each be preceded by a single-sideband suppressed carrier modulator operating at $[0, 1, 3] \times \Omega_0$ to impart the necessary frequency shift.

The target intensity back-scatter reflectivity profile can be decomposed into spatial frequencies in the Fourier domain (corresponding to a spatial Fourier transform), forming an equivalent Fourier-space representation of the target. If sufficient samples of the complex Fourier-space representation can be obtained, the real-space image can be reconstructed by a simple Fourier transform in the ideal case, and by an appropriate reconstruction algorithm in the realistic usage case [32,36].

The $\mathcal{F}$-BASIS approach interrogates individual spatial frequencies of the target's Fourier-space representation using the projected, moving fringe patterns. Each fringe pattern creates a back-scattered return that "blinks" at its unique beat frequency. The amplitude and phase of this blinking encode the amplitude and phase of the corresponding complex spatial Fourier component of the target's intensity reflectivity profile. Since each spatial frequency is tagged with a unique temporal frequency, all fringe patterns can be simultaneously projected onto the target. The RX OPA collects this back-scattered light and uses a high-speed detector to resolve all of the difference frequency beat notes [Fig. 2(bi)]. The amplitudes and phases of the beat notes are extracted using a temporal Fourier transform [Fig. 2(bii)] from which complex samples are taken at the beat note peaks and used to populate samples of the objects spatial frequency representation with appropriate Hermitian symmetry [Fig. 2(biii)]. An inverse spatial Fourier transform, or reconstruction algorithm [36], then generates a real-space image of the reflectivity profile of the illuminated spot [Fig. 2(biv)].

The general case, an array with N non-redundantly spaced emitters in 2D, projects $N(N-1)/2$ unique fringe patterns onto the target. Such non-redundant arrays are thereby able to sample images with a large number of degrees of freedom as compared to a fully packed transmitter array using, e.g., raster scanning [3]. For sparse arrays, the number of emitters N needed to obtain an M pixel image scales as $N \propto \sqrt{M}$ whereas fully populated arrays scale as $N \propto M$, highlighting the advantage of increased resolution using sparse aperture imaging techniques with a minimum possible number of transmitters. Notably, the achievable resolution is identical to that obtained by a fully populated aperture of the same size—an array of width W can resolve a far-field target down to $\lambda z/W$—and the full OPA FOV can be utilized. For additional details on the resolution and FOV, see Supplement 1. Sparse aperture imaging in the Fourier domain thereby reduces the number of elements which must be controlled beyond what can be achieved by fully populated arrays and real-space imaging systems, without compromising the resolution, as well as simplifying chip layout [11]. For large arrays with thousands or even millions of elements, control complexity may become the limiting factor on aperture size. In this case, spare aperture techniques can achieve significantly higher resolution and much larger apertures than fully populated aperture approaches.

A key distinction can be made between the active Fourier-basis *illumination* technique proposed here and the common passive *reception*-based techniques such as synthesis imaging in radio astronomy or a recent integrated photonic demonstration [28]. While much of the analysis is identical because transmission and reception are entirely equivalent in reciprocal systems, active illumination is preferable in two key aspects. First, actively illuminated targets can benefit from higher signals as well as background suppression using a bandpass filter. Second, active illumination allows for the extraction of additional information about the target, in particular lidar ranging and velocimetry [37]. While we do not discuss the application of $\mathcal{F}$-BASIS to ranging in this work, the ability to extract range information (3D imaging) using this technique [37] is a key motivation for its adoption over passive imaging.

A key practical advantage of $\mathcal{F}$-BASIS as applied to OPAs is the ability to obtain diffraction-limited image quality *without* first cohering the phases of all the emitters. This is in stark contrast to the standard OPA imaging approach, raster scan imaging, in which all elements must have exact phase alignment to form a diffraction-limited spot on the target. This is an Achilles' heel and major unsolved problem for scaling integrated photonic OPA-based approaches to large apertures. $\mathcal{F}$-BASIS can correct for the unknown phases of each emitter post-measurement with a self-calibration algorithm [31,32] so long as the unknown phases remain constant within a single imaging "shot". The self-calibration algorithm requires minimal redundancy in the array to be cohered in order to function, and therefore is not compatible with conventional dense 2D arrays of elements.

3. THEORY OF $\mathcal{F}$-BASIS WITH OPAs

In this section, we derive the basic equations needed to analyze the $\mathcal{F}$-BASIS approach within the context of long-distance imaging using a 2D array of emitters. An in-depth derivation and analysis of $\mathcal{F}$-BASIS, initially conceived in the context of microscopy, can be found in [29,38].

As mentioned in Section 2, this paper does not focus on implementing $\mathcal{F}$-BASIS in a single OPA, but rather as a "tiled aperture" comprising an array of OPA "tiles". In this modality, we use a two-level hierarchy of imaging: imaging with a large FOV uses a raster scan approach where each OPA tile steers in two dimensions (raster scans) to a spot [Fig. 1(c), top]; within the spot cast by a single tile, the second imaging level occurs in the form of $\mathcal{F}$-BASIS [Fig. 2(c), bottom] when enhanced resolution within the single-tile spot is desired. By stitching these $\mathcal{F}$-BASIS images (one per raster scan spot) together, a composite image is formed with both the large FOV of a single OPA tile and the high resolution afforded by the full size of the tiled aperture. The analysis followed here is equally applicable to a single OPA composed of an array of emitters, in which the single OPA forgoes raster scanning entirely and images solely using $\mathcal{F}$-BASIS.

We consider the case of a 2D emitter array where each emitter has a unique frequency shift generated by, e.g., a single-sideband suppressed carrier (SSB-SC) modulator. The simplest case is to only "turn on" one pair of emitters, each with its unique frequency, which generates a single moving spatial fringe pattern in the far field. The derivation follows this simple case, and the general result with simultaneous illumination with all fringe patterns from a sparse non-redundant array follows directly.

We assume a rectangular grid of emitters where the field at the chip surface can be modeled as a rectangular window with constant phase and amplitude. The excited field in the OPA plane can then be written as

$$U_A(\vec{r}_T, t; z=0) = \left[\mathrm{rect}\left(\frac{\vec{r}_T\cdot\hat{x}}{w_x}\right)\mathrm{rect}\left(\frac{\vec{r}_T\cdot\hat{y}}{w_y}\right)\right] * \left[\delta\left(\vec{r}_T-\vec{r}_{T1}\right)e^{j\omega_1 t}+\delta\left(\vec{r}_T-\vec{r}_{T2}\right)e^{j\omega_2 t}\right] + \text{c.c.}, \tag{1}$$

where $\vec{r}_T = (x, y)$, each beam-steering OPA tile emitter has size $w_x \times w_y$, and two emitters are excited at aperture-plane locations $\vec{r}_{T1} = (x_1, y_1)$ and $\vec{r}_{T2} = (x_2, y_2)$ with corresponding frequencies $\omega_1 \equiv \omega_0 + \Omega_1$ and $\omega_2 \equiv \omega_0 + \Omega_2$ for an input optical carrier at ω_0. For constant pitch arrays, these locations can be replaced with integer coordinates (m_i, n_i) and corresponding pitches Λ_x, Λ_y such as $\vec{r}_{Ti} = (m_i\Lambda_x, n_i\Lambda_y)$.

The incident field on the target plane in the far field of the OPA array, using the Fraunhofer approximation, is

$$U_{FF}(\vec{r}_T, t; z) = e^{-j\pi r^2/\lambda z}\operatorname{sinc}\left(\frac{w_x\vec{r}_T\cdot\hat{x}}{\lambda z}\right)\operatorname{sinc}\left(\frac{w_y\vec{r}_T\cdot\hat{y}}{\lambda z}\right) \cdot \left(e^{-j[\vec{K}_1\cdot\vec{r}_T-\omega_1 t]} + e^{-j[\vec{K}_2\cdot\vec{r}_T-\omega_2 t]}\right) + \text{c.c.}, \tag{2}$$

where we have defined $\vec{K}_i \equiv 2\pi\vec{r}_{Ti}/\lambda z$ and $\lambda = \lambda_0/n$ is the effective wavelength in the propagation medium. This coherent illumination profile multiplies by the target intensity reflectivity profile $R(\vec{r}_T)$ and back-scatters a time-varying intensity distribution, which at the target can be represented as

$$I_R(\vec{r}_T, t; z) = R(\vec{r}_T)\operatorname{sinc}^2\left(\frac{w_x\vec{r}_T\cdot\hat{x}}{\lambda z}\right)\operatorname{sinc}^2\left(\frac{w_y\vec{r}_T\cdot\hat{y}}{\lambda z}\right) \cdot (1 + \cos[\Delta\vec{K}\cdot\vec{r}_T - \Delta\Omega t]), \tag{3}$$

where we have defined $\Delta\vec{K} = \vec{K}_1 - \vec{K}_2$ and $\Delta\Omega = \Omega_1 - \Omega_2$. A rough target surface will cause this to be scattered in all directions and propagate back to the receiver, producing a blinking speckle field with speckle correlation length $\Lambda(x/w_x, y/w_y)$ (where Λ here denotes the unit width triangle function).

The detected current i_D generated by the back-scattered light, collected by a standard incoherent detector, is directly proportional to the intensity on the illuminated target: $i_D(t) \propto \iint I_R \mathrm{d}\vec{r}_T$, see Supplement 1 for a more detailed derivation. The detection, and corresponding integration over the incident field, is most easily evaluated in the Fourier domain by taking the DC component of the spatial Fourier spectrum: $\iint_{-\infty}^{\infty} f(\vec{r}_T)\mathrm{d}\vec{r}_T = \mathcal{F}\{f(\vec{r}_T)\}_{\vec{K}=(0,0)}$. We can therefore benefit from writing the detected current in the spatial Fourier domain, dropping scaling factors, as

$$i_D(t) = \mathcal{F}\{\mathcal{F}^{-1}\{\mathcal{I}_R(\vec{K})\}\}_{\vec{K}=(0,0)}, \tag{4}$$

where the Fourier transform of the reflected intensity is denoted by $\mathcal{I}_R(\vec{K}) = \mathcal{F}\{I_R(\vec{r}_T)\}$.

We now define a windowed reflectivity function, which combines the sinc beam projected by a single emitter onto the target and the target's reflectivity, as

$$R'(\vec{r}_T; z) = R(\vec{r}_T)\operatorname{sinc}^2\left(\frac{w_x\vec{r}_T\cdot\hat{x}}{\lambda z}\right)\operatorname{sinc}^2\left(\frac{w_y\vec{r}_T\cdot\hat{y}}{\lambda z}\right), \tag{5}$$

with Fourier transform representation $\mathcal{R}'(\vec{K}) = \mathcal{F}\{R'(\vec{r}_T)\}$. Noting that the combination of a Fourier transform and an inverse Fourier transform $(\mathcal{F}\mathcal{F}^{-1})$ is the identity operation, we can evaluate the detector current as

$$\begin{aligned} i_D(t) &= \mathcal{R}'(0,0) + A\cos(\Delta\Omega t + \phi), \\ A &= |\mathcal{R}'(\Delta\vec{K})|, \\ \phi &= \arg[\mathcal{R}'(\Delta\vec{K})], \end{aligned} \tag{6}$$

where we have restricted the target intensity reflectivity to be a real function. We therefore see that the amplitude and phase of the temporal sinusoid component carry the spatial frequency information of the windowed target, tagged with the beat frequency.

This technique captures 2D image information in the Fourier domain using the spatial periodicity of the fringes. Notably, the same concept can be applied for 3D imaging (lidar ranging) [37]. This 3D $\mathcal{F}$-BASIS utilizes the tilt of the 2D fringe pattern along the range dimension to measure Fourier components in all three dimensions and correspondingly reconstructs a 3D, range-resolved image. See [37] for further details.

4. DEMONSTRATION OF $\mathcal{F}$-BASIS IMAGING WITH OPAs

In this paper, we demonstrate integrated photonic $\mathcal{F}$-BASIS imaging for the first time to our knowledge. We use a tiled aperture and an array of OPAs, and reconstruct a "super-resolved" 1D image entirely within the spot of a single OPA tile. Notably, the resolution obtained by the $\mathcal{F}$-BASIS is not higher than that allowed by the diffraction limit of the entire array of OPAs, but can be substantially better than the diffraction limit of a single OPA tile. We fabricated a 2D L-shaped array of OPAs on a single $9 \times 5\ \mathrm{mm}^2$ silicon photonic chip, shown in Fig. 3(a). A single OPA tile is shown in Fig. 3(b). We only use a 1D sparse sub-array for this experiment, which generates a set of 11 fringe patterns. Scrolling these fringe patterns across the target creates a time-varying signal at the detector which has an amplitude and phase corresponding to a spatial frequency of the target as described in Section 3, and the image is reconstructed from the light scattered by the target, encoded by these spatial frequencies.

A. Imaging System Implementation

The $\mathcal{F}$-BASIS imaging system consists of a 12×1 array of $1 \times 0.5\ \mathrm{mm}^2$ OPA tiles of which the populated locations (in the context of this experiment) are (0, 1, 4, 7, 9, 11), highlighted in Fig. 3(a). The non-populated locations are used for other designs on the chip, but could equally well be used as receiver locations for same-chip imaging. This array layout can access all 11 possible fringe patterns, but does so at the cost of a small amount of redundancy (e.g., the fringe pattern created by 7 and 9 is redundant with that of 9 and 11).

For the purposes of this experiment, we demonstrate $\mathcal{F}$-BASIS imaging within the spot of a single SOPA at broadside. This sub-spot imaging procedure can then be performed for any spot within the FOV by raster scanning. These sub-spot images can be stitched together to form a super-resolved image encompassing the entire FOV of a single OPA. As discussed in Supplement 1, there are some simple corrections needed at different steering angles in order to utilize $\mathcal{F}$-BASIS at arbitrary angles. Here, we demonstrate image reconstruction for a single raster scan spot for simplicity.

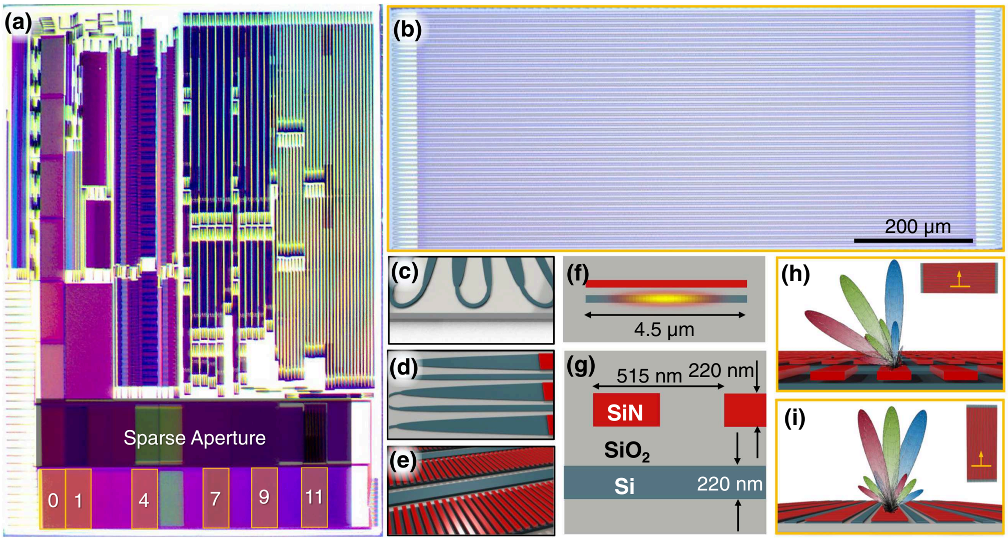

Fig. 3. Fabricated multi-OPA aperture with details on component OPAs. (a) Integrated photonic chip with the (identical) SOPAs composing the sparse tiled aperture highlighted in gold. (b) Microscope image of a single SOPA from the tiled aperture. (c) Rendering of the adiabatic bends. (d) Rendering of adiabatic tapers. (e) Rendering of silicon nitride gratings above the silicon layer. (f) Grating cross-section denoting the waveguide width and with excited lowest-order optical mode overlaid. Separation between waveguide and grating teeth is not to scale. (g) Process layer stack with device layer thicknesses and grating period denoted. (h) Wavelength steering along a grating; gold bar in inset denotes cross-section location. (i) Wavelength steering orthogonal to the gratings; gold bar in inset denotes cross-section location.

B. Serpentine OPA

We use a serpentine OPA (SOPA) tile design which was developed recently within our group [17,33]. The SOPA is a passive OPA that uses serial interconnection of grating rows to raster scan in 2D using laser wavelength tuning alone. The SOPAs used in the $\mathcal{F}$-BASIS imaging system are an updated design relative to our first demonstration in [17], and one of the six identical SOPAs used here is shown in Fig. 3(b). This design has a 900 µm long grating waveguide, 48 such grating waveguide rows, an 8 µm grating-to-grating pitch, 4.5 µm wide gratings, and 1.5 µm wide flyback waveguides. Renderings of the Euler bends, adiabatic tapers, and nitride overclad gratings comprising the SOPA are shown in Figs. 3(c)–3(e), respectively. The wide waveguides and fundamental mode excitation minimize propagation losses and undesired grating lobes [see Fig. 3(f)]; a 515 nm grating tooth pitch is used to emit vertically at a wavelength of 1450 nm so as to avoid back-reflections in the 1450–1650 nm scan range. Relevant features of the layer stack, including device layer thickness, are shown in Fig. 3(g).

The key OPA functionality of the SOPA design is the use of wavelength to control the beam emission angle along both dimensions. Like many recent OPA designs, the long gratings provide wavelength steering along the grating dimension due to the inherent dispersion. Large shifts in wavelength (∼40 GHz, ∼0.3 nm) change the beam emission angle by one resolvable spot along this dimension [Fig. 3(h)]. Wavelength steering along the orthogonal dimension is accomplished using a serpentine delay line in conjunction with weak gratings, which routes the output of one grating to the input of the adjacent grating. This structure creates the same wavelength-dependent emission angle as an arrayed waveguide grating (AWG) input such as in [2], while avoiding the additional space occupied by the multiple delay line inputs. The long delay between grating inputs results in only small wavelength shifts (∼1.5 GHz, ∼0.01 nm) changing the beam emission angle along this row-to-row dimension by one resolvable spot [Fig. 3(i)]. The combination of the serpentine structure with weak, long gratings therefore allows the SOPA to beam-steer in 2D using only wavelength tuning. For further details, see [17]. We have previously demonstrated the basic functionalities of a tiled aperture composed of SOPAs using simultaneous coherent emission from two tiles [17,34] as well as simultaneous transmit/receive using a pair of these SOPA tiles [39].

C. Experimental Setup

Our experimental setup is shown in Fig. 4. The test chip is attached to a TEC (thermoelectric cooler) to maintain a constant 22.5 °C temperature and avoid long-term angular drift of the beam with temperature. In our setup, two SOPA tiles are addressed at a time using a fiber-coupled wavelength-tunable laser operated at 1550 nm, which is passed through a 50:50 splitter and routed to a fiber V-groove coupler. At this wavelength, the SOPAs emit at approximately -18° relative to chip-normal, and a mirror is used to reflect the beams into the plane of the chip.

In order to generate moving fringes, after the splitter, one arm is phase-modulated with a linear ramp to create a small (∼10 Hz) frequency shift $\Delta\Omega$ between the two arms as discussed in Section 3. The other arm of the splitter is not modulated. As both SOPAs are operated at effectively the same wavelength, their illumination patterns overlap in the far field, creating the slowly moving fringe pattern projected onto the target. In order to generate all the desired fringe pairs, we connect the reference and phase-modulated arms to the corresponding channels of the V-groove (which can in principle

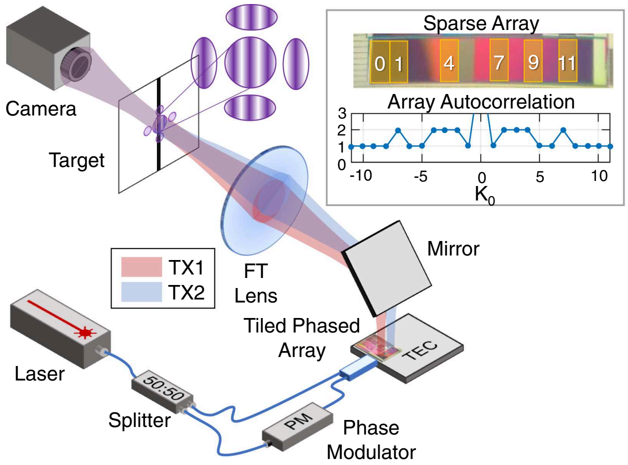

Fig. 4. Experimental setup for demonstration of 1D $\mathcal{F}$-BASIS with a tiled aperture of SOPAs. A laser is split into two channels, where one channel is modulated by a phase-shifter. Both channels then enter into the $\mathcal{F}$-BASIS chips via a V-groove array where, by connecting each channel's fiber to a specific V-groove input, all SOPAs within the sparse array can be addressed. Due to equipment limitations, only two SOPAs are addressed at a time. A thermo-electric cooler is used to stabilize the chip temperature such that all tiles emit to the same far-field spot for the same input wavelength. Interference fringes are projected onto a far-field target (a single opaque line) using a Fourier lens to access the far field. A camera which images the target plane from behind captures the transmitted light and is used both for phase calibration and as a bucket detector by integrating over all camera pixels. Inset: image of sparse SOPA array (top) and the array autocorrelation (bottom) showing that it samples all spatial frequencies, although with some minimal redundancy. FT, Fourier transform; TEC, thermoelectric cooler.

address all SOPA tiles in the sparse array simultaneously). This experimental limitation, that all SOPAs do not emit simultaneously, introduces changing emitter phases during the imaging operation. As mentioned in Section 2, changing emitter phases during the imaging operation unfortunately prevents demonstration of a self-calibration to compensate for unknown emitter phases with this proof-of-principle implementation.

The highest spatial frequency, where the SOPAs are separated by ∼4.5 mm, has a far-field cross-over which is larger than 9 m. This distance is too great to achieve in our lab so the Fourier plane of a lens is used to replicate the far-field condition. We use an IR camera and lens to image the far-field target plane. As a target, we used an opaque wire approximately 100 µm in diameter suspended vertically between two clamps so that the transmitted light can be captured by the camera. The target is used along with an IR camera to provide an alignment mark which allows for the random phase of each OPA pair to be removed from the measurement. A time-series of camera frames is captured for each measurement and the total intensity of each frame is calculated digitally as an analog for the back-scattered intensity which would be detected in an actual far-field imaging experiment, the signal for the $\mathcal{F}$-BASIS method. Using Eq. (6), we extract the amplitude and phase of each Fourier component.

In the envisioned system, integrated SSB-SC frequency shifters preceding each SOPA would generate the non-redundant frequency array using a single seed laser. All TX SOPAs would illuminate the target simultaneously and the back-scattered light would be collected by one or more RX SOPAs, with unknown TX phases corrected for in a post-measurement step using a self-calibration algorithm. For this initial demonstration, which does not have on-chip frequency shifters or a distribution network, the core imaging functionality is demonstrated using a separate detector in the far field to collect sufficient power and correct phase errors pre-measurement. The far-field detector captures the transmitted light rather than the back-scattered light (like an ideal $\mathcal{F}$-BASIS system). Additionally, in this experiment, only a pair of SOPAs transmit at a time, and the beam power of each SOPA on the target is measured individually to account for emission power variation. This setup is therefore an experimental emulation of the full system.

D. Image Reconstruction Results

To reconstruct an image of the target, we sample each spatial frequency of the target sequentially. First, we calibrate the phase of each fringe pattern using the target as an alignment mark [Fig. 5(a)]. In this demonstration, we do not use any phase-recovery algorithms for image reconstruction, and therefore it is essential that all fringes have a constant phase reference for accurate image reconstruction. The fringe patterns at all 11 spatial frequencies are shown in Fig. 5(b) after phase calibration. The projected spot is not a perfect sinc due to phase errors across the SOPA tiles, resulting in sidelobes along the horizontal dimension. These sidelobes do not inhibit fringe formation, but do result in cross-talk between adjacent spot images. The periodicity, phase, and visibility of the generated fringes are all of sufficient quality to reconstruct the line target demonstrated here; improved spot quality (phase and power uniformity within the projected spot) will be required for high-fidelity reconstructions of complex images in an actual $\mathcal{F}$-BASIS SOPA tiled array imaging system.

A phase ramp modulation is applied between the two arms, causing the fringe to scroll across the target, in this case at only a few Hz; the camera provides time-resolved imaging of this scrolling [Fig. 5(c), top]. Digital integration over each frame of the resulting movie yields an intensity measurement versus time which provides an emulated signal (for this initial demonstration) which is directly proportional to the desired signal—a bucket detector or RX SOPA capturing the time-varying back-scattered intensity. A single period of the $k_x = 4K_0$ signal is shown in Fig. 5(c), bottom, where the marked points correspond to the intensity measured for each of the five example camera frames as the fringe scrolls from left to right across the camera. For each spatial frequency, the amplitude and phase of this intensity signal is extracted and inserted as an appropriate complex sample in the Fourier domain representation of the target [Fig. 5(d)]. Each spatial frequency measurement contributes both a positive and negative frequency component, with appropriate conjugate phases, since the target's intensity reflectivity is being sampled (which is positive real). A real-space image reconstruction is then obtained by a simple inverse Fourier transform [Fig. 5(e)]. The line target, shown in red, is clearly not resolvable by the spot of a single SOPA (green). However, the $\mathcal{F}$-BASIS imaging system is able to approximately resolve the line target (blue) with a resolution 11× higher than a single SOPA using

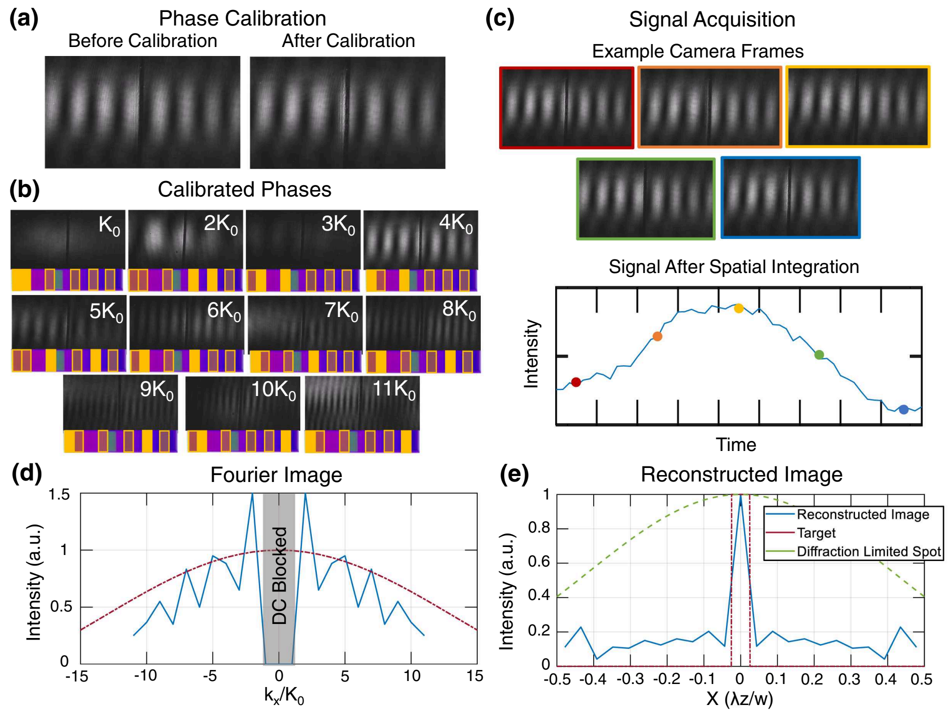

Fig. 5. Experimental demonstration of line target reconstruction using a sparse array of OPAs. (a) An alignment mark is used in the target plane correct for the initially unknown phase of each emitter pair. (b) Images of calibrated phase for each emitter pair, showing all 11 spatial periods sampled in this experiment. (c) Signal acquisition for a single spatial period ($4K_0$) after phase calibration. Phase modulation is applied to one SOPA to sweep the fringes across the target, and the camera captures this fringe motion (five example images shown). Digital integration of the total intensity of each camera frame yields a time-varying intensity (bottom) which is the $\mathcal{F}$-BASIS signal. (d) This signal acquisition is performed for each unique spatial frequency, building up a spatial Fourier domain representation of the target (blue, solid). The ground-truth of the target's spatial Fourier distribution is shown in red (dash-dot). (e) An inverse Fourier transform reconstructs an image (blue, solid) of the target (red, dash-dot), demonstrating 11× resolution enhancement over the diffraction-limited spot of a single SOPA (green, dashed).

only six SOPAs tiles, whose arrangement spans an 11× wider tiled aperture than the single tile width.

5. DISCUSSION AND CONCLUSION

As can be seen from the experimental demonstration, $\mathcal{F}$-BASIS is capable of significantly increased resolution compared to a single SOPA tile. This enables the use of tiled arrays of OPAs (like SOPAs) to scale to large apertures by drastically reducing the number of OPAs required to achieve the resolution associated with a large composite aperture. This initial demonstration provides a first step towards achieving this goal, proving the capability to image targets using an $\mathcal{F}$-BASIS approach with OPAs. Future work is needed to extend this capability, including use of 2D sparse arrays, on-chip splitter trees, and phase modulators, detection of back-scattered light with OPA receivers, combination with ranging techniques for 3D image reconstruction, and incorporation of the self-calibration algorithm. Together, these extensions will significantly improve the $\mathcal{F}$-BASIS approach and, with the use of a self-calibration algorithm, the presence of phase errors due to fabrication or thermal variations can also be corrected using only the detected back-scatter from the target without any cohering reference. More importantly, we believe that this approach opens a path to scaling integrated photonic coherent imagers to large (cm-scale) apertures. The sensitivities of integrated photonics make direct phase cohering of large apertures extremely difficult in terms of complexity, power, and computing cost. Thus, approaches like $\mathcal{F}$-BASIS combined with self-calibration which alleviates the phase-cohering issue could prove revolutionary for optical imaging by leveraging the most scalable known technology, CMOS, to large-aperture, integrated photonic imaging.

The main limitations of the results presented in this paper are tied to the particular implementation of SOPAs used for this demonstration, which do not achieve diffraction-limited performance. The phase errors within each SOPA are a result of the ~10 cm path length folded up into the compact serpentine combined with fabrication dimensional variations, particularly in waveguide layer thicknesses that affect the fundamental mode propagation constant. Some future SOPA designs already in development include heaters integrated into the SOPAs to correct for these phase errors, while other SOPA designs are significantly smaller to decrease sensitivity to fabrication variations. Both of these approaches should enable near diffraction-limited performance of an individual SOPA and drastically reduce sidelobe levels, improving the fidelity of the $\mathcal{F}$-BASIS imaging.

In addition, the experimental and equipment limitations prevented demonstration of self-calibration of the $\mathcal{F}$-BASIS demonstration in this initial work. Improved experimental setups, particularly a fully integrated chip where a single fiber input is distributed on-chip and modulated, would enable a self-calibrated $\mathcal{F}$-BASIS imaging demonstration. Such a chip would enable single-shot measurement by emitting from all SOPAs simultaneously and allowing for use of a self-calibration algorithm, avoiding the artificial phase errors and path-length mismatch from reconnecting fibers endemic to this initial demonstration.

In this paper, we used a sparse array of SOPAs to demonstrate a Fourier-basis active illumination imaging technique, $\mathcal{F}$-BASIS. Using a sparse array with six populated locations of an 11-point linear array of OPA tile "slots", we demonstrate reconstruction of a line target with 11× resolution enhancement over a single constituent OPA. This demonstration is, to our knowledge, the first demonstration of imaging using multiple integrated photonic OPAs. These results are a critical step forward for demonstrating imaging with OPAs, in particular for high-resolution and long-range applications where arrays containing many OPAs will be needed.

Funding. David and Lucile Packard Foundation (2012-38222); National Defense Science and Engineering Graduate (GS00Q14OADS139); National Science Foundation (1144083).

Acknowledgment. Portions of this work were presented at the Digital Holography and 3D Imaging Meeting in 2019 in the paper *Super-Resolved Interferometric Imaging with a Self-Cohering Si-Photonic Beam-Steering LIDAR Array*, M5A.1 [40] as well as at the OSA Imaging/Sensing Congress in 2020 in the paper *Structured Illumination with Optical Phased Arrays (OPAs): First Demonstration of Multi-OPA Imaging*, CF3C.2 [41]. Chip layout was carried out using an academic license of Luceda Photonics IPKISS.

Disclosures. M. Popović: Ayar Labs (I, C).

Data Availability. Data underlying the results presented in this paper are not publicly available at this time but may be obtained from the authors upon reasonable request.

Supplemental document. See Supplement 1 for supporting content.

REFERENCES

1. J. Hecht, "Lidar for self-driving cars," Opt. Photon. News **29**, 26–33 (2018).
2. K. Van Acoleyen, H. Rogier, and R. Baets, "Two-dimensional optical phased array antenna on silicon-on-insulator," Opt. Express **18**, 13655–13660 (2010).
3. J. Sun, E. Timurdogan, A. Yaacobi, E. S. Hosseini, and M. R. Watts, "Large-scale nanophotonic phased array," Nature **493**, 195–199 (2013).
4. D. Kwong, A. Hosseini, J. Covey, Y. Zhang, X. Xu, H. Subbaraman, and R. T. Chen, "On-chip silicon optical phased array for two-dimensional beam steering," Opt. Lett. **39**, 941–944 (2014).
5. H. Abediasl and H. Hashemi, "Monolithic optical phased-array transceiver in a standard SOI CMOS process," Opt. Express **23**, 6509–6519 (2015).
6. J. Hulme, J. Doylend, M. Heck, J. Peters, M. Davenport, J. Bovington, L. Coldren, and J. Bowers, "Fully integrated hybrid silicon two dimensional beam scanner," Opt. Express **23**, 5861–5874 (2015).
7. F. Aflatouni, B. Abiri, A. Rekhi, and A. Hajimiri, "Nanophotonic projection system," Opt. Express **23**, 21012–21022 (2015).
8. D. N. Hutchison, J. Sun, J. K. Doylend, R. Kumar, J. Heck, W. Kim, C. T. Phare, A. Feshali, and H. Rong, "High-resolution aliasing-free optical beam steering," Optica **3**, 887–890 (2016).
9. S. Spector, B. Lane, M. Watts, L. Benney, J. Delva, A. Hare, A. Kelsey, J. Mlynarczyk, E. Hosseini, C. Poulton, and J. Laine, "Broadband imaging and wireless communication with an optical phased array," in *CLEO: Science and Innovations* (OSA, 2018), paper SM3I–7.
10. R. Fatemi, B. Abiri, A. Khachaturian, and A. Hajimiri, "High sensitivity active flat optics optical phased array receiver with a two-dimensional aperture," Opt. Express **26**, 29983–29999 (2018).
11. R. Fatemi, A. Khachaturian, and A. Hajimiri, "A nonuniform sparse 2-D large-FOV optical phased array with a low-power PWM drive," IEEE J. Solid-State Circuits **54**, 1200–1215 (2019).
12. Y. Kohno, K. Komatsu, R. Tang, Y. Ozeki, Y. Nakano, and T. Tanemura, "Ghost imaging using a large-scale silicon photonic phased array chip," Opt. Express **27**, 3817–3823 (2019).
13. C. V. Poulton, M. J. Byrd, P. Russo, E. Timurdogan, M. Khandaker, D. Vermeulen, and M. R. Watts, "Long-range lidar and free-space data communication with high-performance optical phased arrays," IEEE J. Sel. Top. Quantum Electron. **25**, 7700108 (2019).
14. W. Xie, T. Komljenovic, J. Huang, M. Tran, M. Davenport, A. Torres, P. Pintus, and J. Bowers, "Heterogeneous silicon photonics sensing for autonomous cars," Opt. Express **27**, 3642–3663 (2019).
15. W. D. Sacher, X. Liu, F.-D. Chen, H. Moradi-Chameh, I. F. Almog, T. Lordello, M. Chang, A. Naderian, T. M. Fowler, E. Segev, T. Xue, S. Mahallati, T. A. Valiante, L. C. Moreaux, J. K. S. Poon, and M. L. Roukes, "Beam-steering nanophotonic phased-array neural probes," in *CLEO: Applications and Technology* (OSA, 2019), paper ATh4I–4.
16. Y. Zhang, Y.-C. Ling, K. Zhang, C. Gentry, D. Sadighi, G. Whaley, J. Colosimo, P. Suni, and S. B. Yoo, "Sub-wavelength-pitch silicon-photonic optical phased array for large field-of-regard coherent optical beam steering," Opt. Express **27**, 1929–1940 (2019).
17. N. Dostart, B. Zhang, A. Khilo, M. Brand, K. A. Qubaisi, D. Onural, D. Feldkhun, K. H. Wagner, and M. A. Popović, "Serpentine optical phased arrays for scalable integrated photonic lidar beam steering," Optica **7**, 726–733 (2020).
18. H. Ito, Y. Kusunoki, J. Maeda, D. Akiyama, N. Kodama, H. Abe, R. Tetsuya, and T. Baba, "Wide beam steering by slow-light waveguide gratings and a prism lens," Optica **7**, 47–52 (2020).
19. S. A. Miller, Y.-C. Chang, C. T. Phare, M. C. Shin, M. Zadka, S. P. Roberts, B. Stern, X. Ji, A. Mohanty, O. A. J. Gordillo, U. D. Dave, and M. Lipson, "Large-scale optical phased array using a low-power multi-pass silicon photonic platform," Optica **7**, 3–6 (2020).
20. Y. Bromberg, O. Katz, and Y. Silberberg, "Ghost imaging with a single detector," Phys. Rev. A **79**, 053840 (2009).
21. D. L. Donoho, "Compressed sensing," IEEE Trans. Inf. Theory **52**, 1289–1306 (2006).
22. T. Komljenovic, R. Helkey, L. Coldren, and J. E. Bowers, "Sparse aperiodic arrays for optical beam forming and lidar," Opt. Express **25**, 2511–2528 (2017).
23. N. J. Miller, M. P. Dierking, and B. D. Duncan, "Optical sparse aperture imaging," Appl. Opt. **46**, 5933–5943 (2007).
24. R. Holmes, S. Ma, A. Bhowmik, and C. Greninger, "Analysis and simulation of a synthetic-aperture technique for imaging through a turbulent medium," J. Opt. Soc. Am. A **13**, 351–364 (1996).
25. W. T. Rhodes, "Time-average Fourier telescopy: a scheme for high-resolution imaging through horizontal-path turbulence," Appl. Opt. **51**, A11–A16 (2012).
26. J. J. Field, D. G. Winters, and R. A. Bartels, "Single-pixel fluorescent imaging with temporally labeled illumination patterns," Optica **3**, 971–974 (2016).
27. F. Cassaing and L. Mugnier, "Optimal sparse apertures for phased-array imaging," Opt. Lett. **43**, 4655–4658 (2018).
28. T. Su, G. Liu, K. E. Badham, S. T. Thurman, R. L. Kendrick, A. Duncan, D. Wuchenich, C. Ogden, G. Chriqui, S. Feng, J. Chun, W. Lai, and S. J. B. Yoo, "Interferometric imaging using Si3N4 photonic integrated circuits for a SPIDER imager," Opt. Express **26**, 12801–12812 (2018).
29. D. Feldkhun and K. H. Wagner, "Doppler encoded excitation pattern tomographic optical microscopy," Appl. Opt. **49**, H47–H63 (2010).
30. D. Feldkhun and K. H. Wagner, "Single-shot afocal three-dimensional microscopy," Opt. Lett. **41**, 3483–3486 (2016).
31. F. R. Schwab, "Adaptive calibration of radio interferometer data," Proc. SPIE **0231**, 18–25 (1980).
32. D. Feldkhun and K. H. Wagner, "Frequency-mapped focus-free F-BASIS 3D microscopy," in *Computational Optical Sensing and Imaging* (OSA, 2015), paper CM1E–2.
33. B. Zhang, N. Dostart, A. Khilo, M. Brand, K. Al Qubaisi, D. Onural, D. Feldkhun, M. A. Popović, and K. Wagner, "Serpentine optical phased array silicon photonic aperture tile with two-dimensional wavelength beam steering," in *Optical Fiber Communication Conference* (OSA, 2019), paper M4E–5.

34. B. Zhang, N. Dostart, M. Brand, A. Khilo, D. Feldkhun, M. A. Popović, and K. Wagner, “Tiled silicon-photonic phased arrays for large-area apertures,” in *CLEO: Science and Innovations* (OSA, 2019), paper SF3N–2.
35. M. J. Golay, “Point arrays having compact, nonredundant autocorrelations,” J. Opt. Soc. Am. **61**, 272–273 (1971).
36. U. Schwarz, “Mathematical-statistical description of the iterative beam removing technique (method CLEAN),” Astron. Astrophys. **65**, 345 (1978).
37. K. Wagner, N. Dostart, K. Ting, B. Zhang, M. Brand, D. Feldkhun, and M. Popović, “3D Fourier synthesis active imaging using a spatio-spectral non-redundant array of silicon-photonic beamsteering tiles,” in *Computational Optical Sensing and Imaging* (OSA, 2020), paper CF1C–5.
38. D. Feldkhun, “Doppler encoded excitation patterning (DEEP) microscopy,” Ph.D. thesis (University of Colorado Boulder, 2010).
39. N. Dostart, M. Brand, B. Zhang, D. Feldkhun, K. Wagner, and M. A. Popović, “Vernier Si-photonic phased array transceiver for grating lobe suppression and extended field-of-view,” in *CLEO: Applications and Technology* (OSA, 2019), paper AW3K–2.
40. K. Wagner, D. Feldkhun, B. Zhang, N. Dostart, M. Brand, and M. Popović, “Super-resolved interferometric imaging with a self-cohering Si-photonic beam-steering lidar array,” in *Digital Holography and Three-Dimensional Imaging* (OSA, 2019), paper M5A–1.
41. N. Dostart, M. Brand, B. Zhang, D. Feldkhun, M. Popović, and K. Wagner, “Structured illumination with optical phased arrays (OPAs): first demonstration of multi-OPA imaging,” in *OSA Imaging/Sensing Congress* (OSA, 2020), paper CF3C.2.